Photoelectron spectroscopic study of the E#e Jahn–Teller effect in the presence of a tunable spin-orbit interaction. II. Rovibronic analysis of the (2)E ground state of CH3Cl+

Journal Article

Author(s):
Grütter, Monika; Merkt, Frédéric (iD)

Photoelectron spectroscopic study of the E⊗e Jahn-Teller effect in the presence of a tunable spin-orbit interaction.

II. Rovibronic analysis of the ^{2}E ground state of CH$_3$Cl$^+$

M. Grütter and F. Merkt

Laboratorium für Physikalische Chemie, ETH Zürich,

CH-8093 Zurich, Switzerland

July 14, 2011

Abstract

The PFI-ZEKE photoelectron spectrum of the CH$_3$Cl$^+$ $\tilde{X}^+$ ^{2}E ← CH$_3$Cl $\tilde{X}$ ^{1}A$_1$ transition was recorded in the range $90\,900 - 93\,400$ cm^{-1} following single-photon excitation from the ground state. The spectrum consists of well-resolved spin-vibronic bands, some of which with partially resolved rotational structure, and provides new information on the combined effects of the Jahn-Teller and spin-orbit interaction in the $\tilde{X}^+$ ^{2}E ground state of CH$_3$Cl$^+$. The analysis of its spin-rovibronic structure reveals a weak linear Jahn-Teller effect along the H$_3$C−Cl bending e mode (ν_6) and enabled the derivation of Jahn-Teller coupling constants along ν_6, rotational constants, and spin-orbit interaction parameters for the $\tilde{X}^+$ ^{2}E ground state of CH$_3$Cl$^+$. The Jahn-Teller effect is dynamical in the ground state of CH$_3$Cl$^+$ and the photoelectron spectrum does not provide evidence for a reduction of the molecular symmetry to C$_s$ symmetry. Weak rotational satellite bands were observed in transitions to several excited vibrational levels of CH$_3$Cl$^+$ and interpreted in terms of the spin-rovibronic photoionization selection rule $\Delta P = P^+ - K = \Lambda - \ell_v + \Sigma$ derived in the analysis of the photoelectron spectrum of CH$_3$I [M. Grütter, J. M. Michaud and F. Merkt, J. Chem. Phys. **134**, 054308 (2011)]. Compared to the ground state of HCl$^+$ ($a = -645(5)$ cm^{-1}), the

spin-orbit splitting is strongly reduced to $a\zeta_e d_{j=1/2,v=0} = -217.5(2.0)$ cm^{-1}. The reduction is primarily attributed to an electronic effect ($\zeta_e = 0.35(4)$) and, to a lesser extent, to the quenching of the spin-orbit interaction by the Jahn-Teller effect ($d_{j=1/2,v=0} = 0.963(20)$).

1 Introduction

The methyl-halide cations in their ^2E electronic ground states are subject to an E⊗e Jahn-Teller interaction and spin-orbit coupling [1, 2, 3, 4], and represent ideal systems with which to study these interactions. The spin-orbit coupling increases by more than one order of magnitude in the series CH_3F^+, CH_3Cl^+, CH_3Br^+ and CH_3I^+, which results in the possibility, already exploited in previous studies [1, 2, 5, 6, 7, 8], of investigating the Jahn-Teller effect in dependence of the spin-orbit coupling strength. Comparison with the isoelectronic neutral molecules CH_3O [9, 10, 11] and CH_3S [9, 12] provides the opportunity of studying the consequences of small changes of the electronic structure on the Jahn-Teller effect and the spin-orbit interaction and their combined influence on the molecular structure and dynamics.

After our report of the photoelectron spectrum of CH_3I [4], this article is the second of a series of articles devoted to the study, by high-resolution photoelectron spectroscopy, of the methyl-halide cations and of the photoionization dynamics of the parent neutral molecules. Compared to earlier work on the methyl-halide cations, the work presented in this article series seeks to obtain and exploit information contained in the rotational structure of the photoelectron spectra in addition to that contained in the spin-vibronic structure. Such information offers the following advantages: It enables one to establish the vibronic symmetry of the cationic states using rovibronic photoionization selection rules, to determine the molecular structure from the rotational constants, and to obtain complementary information on the Jahn-Teller effect from the rotational subband structure as demonstrated in Ref. [4].

The angular momentum coupling hierarchy and the relative strengths of the different interactions in the cation can be directly derived from the rotational structure. The photoelectron spectra of systems subject to weak spin-orbit coupling, such as CH_3F^+ [13], are characterized by spectral patterns typical of ionizing transitions connecting states of the neutral molecule and the cation both characterized by Hund's-case-(b)-type angular momentum coupling. When the spin-orbit coupling is strong, as is the case for CH_3I^+ [4], the rotational intensity distribu-

tions, spectral patterns, and selection rules are very different and conform to ionizing transitions connecting neutral ground states and cationic states characterized by Hund's-case-(b)-type and (a)-type coupling, respectively.

Information contained in the rotational structure of the photoelectron spectra of the methyl halides has only recently become available. Kim and his coworkers and Ng and his coworkers have recorded high-resolution MATI or PFI-ZEKE photoelectron spectra of CH_3Br [14] and CH_3I [15, 16, 17, 18, 19, 20], however, without attempting a systematic investigation of the rotational structures of the photoelectron spectra. The present series of articles on the photoelectron spectra of CH_3I [4], CH_3F [13] and CH_3Cl aims at filling this gap. Within the series of the methyl halides, CH_3Cl represents an intermediate case between CH_3F, the photoelectron spectrum of which hardly contains any signature of spin-orbit coupling but clear signatures of the Jahn-Teller effect, and CH_3I, the photoelectron spectrum of which reveals strong effects of the spin-orbit coupling but only very weak signatures of the Jahn-Teller effect, primarily in the form of rotational subbands [4, 16]. In CH_3Cl^+, the strengths of the Jahn-Teller and spin-orbit interactions are comparable, which renders the photoelectron spectrum more complex to interpret, but also more interesting to study. This complexity has resulted in conflicting or ambiguous assignments (see e.g., Refs. [1, 5, 8]), which this article seeks to clarify. Unambiguous assignments of the spin-vibronic energy levels of CH_3Cl^+ are also expected to help resolving open questions concerning the assignment of the Rydberg spectrum of CH_3Cl (see Refs. [21, 22], and references therein).

2   Experiment

The PFI-ZEKE photoelectron spectrum of the $\tilde{X}^+ \, ^2E \leftarrow \tilde{X} \, ^1A_1$ transition of CH_3Cl was recorded in the range $90\,900 - 93\,400 \text{ cm}^{-1}$ using the tunable vacuum-ultraviolet (VUV) light source described in Ref. [23]. The VUV radiation was generated in a three-color, two-photon-resonant difference-frequency-mixing process in argon. The $3p^5 4p'[1/2]_0 \leftarrow 3p^6 \, (^1S_0)$ two-photon tran-

sition in Ar at 108722.6248 cm^{-1} used to enhance the four-wave-mixing process was accessed using an F$_2$ excimer laser ($\lambda_{\mathrm{Ex}} \approx 157$ nm) and a UV laser with wavelength $\lambda_1 \approx 220$ nm, generated by frequency tripling the output of a dye laser with two subsequent β-barium-borate BBO crystals. To generate tunable VUV radiation of wave number $\tilde{\nu}_{\mathrm{VUV}} = \tilde{\nu}_1 + \tilde{\nu}_{\mathrm{Ex}} - \tilde{\nu}_2$, the tunable output of a second dye laser in the visible range ($\tilde{\nu}_2$) was spatially and temporally overlapped with the beams of wave numbers $\tilde{\nu}_{\mathrm{Ex}}$ and $\tilde{\nu}_1$ and focused at the exit of a pulsed valve used to produce a supersonic jet expansion of pure argon (purity 99.99 %). The laser system, gas pulses and detection electronics were pulsed at a repetition rate of $16\frac{2}{3}$ Hz. All trigger pulses were synchronized to the output signal of the F$_2$ excimer to reduce the effects of its jitter to below 5 ns. The tunable VUV radiation ($\tilde{\nu}_{\mathrm{VUV}}$) was then guided into the photoexcitation chamber via a monochromator grating, which spatially separated the VUV beam from the fundamental beams with wave numbers $\tilde{\nu}_1$, $\tilde{\nu}_2$, and $\tilde{\nu}_{\mathrm{Ex}}$ and from beams generated in other nonlinear processes. The torroidal geometry of the grating enabled the recollimation of the diverging VUV laser beam.

Pure CH$_3$Cl gas (Aldrich, purity 99.5 %) at a stagnation pressure of ≈ 2 bar was introduced into the vacuum system through a pulsed valve (General Valve, Series 9). The methyl chloride gas contained the isotopomers CH$_3^{35}$Cl and CH$_3^{37}$Cl with their natural abundances, i.e., 75.77 % and 24.23 %, respectively. The supersonic gas beam, with a rotational temperature $T_{\mathrm{rot}} \approx$ 12 K, was skimmed and guided into the photoexcitation chamber, where single-photon VUV photoexcitation to the region of the lowest ionization thresholds took place under field-free conditions. To record photoionization spectra, the ions were extracted by an electric-field pulse of 140 Vcm^{-1} applied 1.3 μs after the VUV excitation, and monitored using a microchannel plate (MCP) detector. The pulsed electric field also led to the field-ionization of long-lived high Rydberg states located below the successive ionization thresholds.

To record PFI-ZEKE photoelectron spectra, the signal resulting from the delayed pulsed field ionization of high Rydberg states was monitored as a function of the VUV wave number. The field-ionization pulse sequences, applied $1-3$ μs after the VUV laser pulse, consisted of a positive

discrimination pulse of 1 μs duration followed by a negative field-ionization pulse of 1 μs duration, which also extracted the electrons towards the MCP detector. Two electric-field pulse sequences were employed ((+70 mV/cm, −70 mV/cm) and (+140 mV/cm, −175 mV/cm)) which enabled us to either optimize the signal-to-noise (S/N) ratio at a full width at half maximum (FWHM) of the spectral lines of 1.0 cm^{-1}, or the spectral resolution (FWHM = 0.6 cm^{-1}) at a reduced S/N ratio. The electron or ion signals were transmitted to a digital oscilloscope, averaged over a preset number of experimental cycles, and integrated over selected time windows. The integrated signal, recorded as a function of the VUV wave number, was stored on a personal computer.

The necessity to overlap three distinct laser beams (one of which in the VUV) temporally and spatially in the nonlinear-gas beam led to a VUV intensity of $\sim 10^9$ photons/pulse, i.e., an order of magnitude lower than can be achieved by two-photon resonant four-wave mixing using krypton or xenon as nonlinear media [23]. All PFI-ZEKE and photoionization spectra were calibrated by guiding a small fraction of the tunable laser beam ($\tilde{\nu}_2$) into an optogalvanic cell filled with neon, monitoring the optogalvanic spectrum of neon, and subsequently comparing the positions of the lines of the optogalvanic spectrum of neon with tabulated transition wave numbers [24]. This procedure resulted in a wave-number accuracy of better than 0.2 cm^{-1}. Including the uncertainty of the energy shifts of the ionization thresholds induced by the pulsed electric fields [25], the overall absolute calibration uncertainty is ±0.5 cm^{-1}.

3 Spin-rovibronic coupling in the ^{2}E electronic ground state of CH$_3$Cl$^+$

Our analysis of the photoelectron spectrum of CH$_3$Cl is restricted to the treatment of the E ⊗ e Jahn-Teller effect and spin-orbit coupling in the $\tilde{X}^+$ ^{2}E ground state of CH$_3$Cl$^+$. The pseudo-Jahn-Teller effect [26, 27, 28] coupling the $\tilde{X}^+$ ^{2}E ground state to the higher-lying $\tilde{A}^+$ ^{2}A$_1$ electronic state of CH$_3$Cl$^+$ was neglected, which is a reasonable approximation in the region of low internal energies of the methyl-chloride cation ($0 - 2500$ cm^{-1}, see Fig. 2) relevant to the

present study. Indeed, the $\tilde{A}^+$ $^2A_1$ electronic state, which results from the ionization out of the σ_{C-Cl} molecular orbital, is located more than $20\,000$ cm^{-1} above the $\tilde{X}^+$ ^2E ground state [1, 5]. Photoelectron spectroscopy from the ground state of the methyl halides CH_3X (X=F,Cl,Br,I) does not provide access to the ylidion isomers (H_2CXH^+), although these are predicted to be more stable than the methyl-halide cations [29, 30] and can be isolated and observed in solid neon matrices [7].

3.1 Vibronic and spin-orbit coupling in the ^2E electronic ground state

The electronic motion in the doubly degenerate $\tilde{X}^+$ ^2E electronic ground state of CH_3Cl^+, with the two possible projections ($|\Lambda = \pm 1\rangle$) of the electronic orbital angular momentum onto the z-axis of the molecule-fixed reference frame, is coupled to the Jahn-Teller-active doubly-degenerate e vibrational modes, described by $|v_i, \ell_{v_i}\rangle$ ($i = 4, 5, 6$, and v_i and ℓ_{v_i} represent the vibrational quantum number and vibrational angular momentum quantum number, respectively) [9, 26, 31]. The linear E⊗e Jahn-Teller effect leads to a distortion of the molecular geometry to C_s symmetry structures and to the formation of a circular trough of isoenergetic C_s equilibrium structures on the ground-state potential energy surface [26], centered at the position of the conical intersection of C_{3v} symmetry. A further distortion, arising from the quadratic Jahn-Teller effect and resulting in the formation of three localized minima of C_s symmetry on the potential energy surface [26], may be treated as a weak perturbation if the linear Jahn-Teller stabilization energy [9]

$$E_{JT} = \sum_i E_{JT,i} = \sum_i hc\omega_i D_i, \tag{1}$$

is significantly smaller than the zero-point energy of the system, i.e., if $E_{JT,i} << \omega_i$ (ω_i represents the harmonic wave number of the ith mode of e symmetry). In Eq. (1), the parameter D_i represents the dimensionless linear Jahn-Teller coupling strength of the ith e mode. The present treatment is restricted to the linear coupling along a single Jahn-Teller active e mode (ν_6). The spin-vibronic interaction is conveniently described in matrix form using the spin-vibronic basis $|v, \ell_v, \Lambda, \Sigma\rangle$ [9]. This basis set is infinite and must be truncated in the calculations at values of

v large enough to ensure convergence of the vibronic states of interest.

The effective spin-vibronic coupling Hamiltonian $\hat{H}_{\text{eff}}$ used in the analysis is of the form [9]

$$\hat{H}_{\text{eff}} = \hat{H}_{\text{harm}} + \hat{H}_{\text{JT}} + \hat{H}_{\text{SO}}. \tag{2}$$

The effective spin-orbit coupling Hamiltonian $\left(\hat{H}_{\text{SO}}\right)$ and the Hamiltonian describing the vibrational structure of the Jahn-Teller-active mode in the harmonic-oscillator approximation $\left(\hat{H}_{\text{harm}}\right)$ are diagonal with matrix elements [9]

$$\langle v, \ell_v, \Lambda, \Sigma | \frac{\hbar^2}{hc} \left[\hat{H}_{\text{harm}} + \hat{H}_{\text{SO}} \right] |v, \ell_v, \Lambda, \Sigma \rangle = \omega(v + 1) + a\zeta_{\text{e}}\Lambda\Sigma. \tag{3}$$

In Eq. (3), the zero-point energy in the other modes of the system is not explicitly considered, because a relative energy scale suffices for the description of the energy level structure of the cation. The Hamiltonian $\left(\hat{H}_{\text{JT}}\right)$ describing the linear Jahn-Teller effect possesses off-diagonal elements [9]

$$\langle v, \ell_v, \Lambda = -1, \Sigma | \frac{\hbar^2}{hc} \hat{H}_{\text{JT}} | v' = v - 1, \ell'_{v'} = \ell_v - 1, \Lambda = +1, \Sigma \rangle$$
$$= \omega \sqrt{D(v' + \ell'_{v'} + 2)} \tag{4}$$

$$\langle v, \ell_v, \Lambda = -1, \Sigma | \frac{\hbar^2}{hc} \hat{H}_{\text{JT}} | v' = v + 1, \ell'_{v'} = \ell_v - 1, \Lambda = +1, \Sigma \rangle$$
$$= \omega \sqrt{D(v' - \ell'_{v'})} \tag{5}$$

$$\langle v, \ell_v, \Lambda = +1, \Sigma | \frac{\hbar^2}{hc} \hat{H}_{\text{JT}} | v' = v - 1, \ell'_{v'} = \ell_v + 1, \Lambda = -1, \Sigma \rangle$$
$$= \omega \sqrt{D(v' - \ell'_{v'} + 2)} \tag{6}$$

$$\langle v, \ell_v, \Lambda = +1, \Sigma | \frac{\hbar^2}{hc} \hat{H}_{\text{JT}} | v' = v + 1, \ell'_{v'} = \ell_v + 1, \Lambda = -1, \Sigma \rangle$$
$$= \omega \sqrt{D(v' + \ell'_{v'})}, \tag{7}$$

which couple basis states having the same value of the Jahn-Teller quantum number [4, 9]

$$j = \ell_v + \frac{1}{2}\Lambda. \tag{8}$$

8

Consequently, the spin-vibronic interactions can be represented by matrices that are block-diagonal in both j and Σ. To each matrix block with a given j value corresponds a matrix block with $j' = -j$ having the same eigenvalues. This double degeneracy of the spin-vibronic states results from Kramers' degeneracy in systems with half-integer angular momentum [32], and enables one to consider only the matrix block corresponding to positive j values.

The Jahn-Teller interaction results in a quenching of the observable effects of the spin-orbit interaction. The spin-orbit Hamiltonian $\hat{H}_{SO}$ in the presence of a Jahn-Teller interaction can be expressed as [4, 9]

$$\frac{\hbar^2}{hc}\hat{H}_{SO}|j,\Sigma\rangle = a\zeta_{e}d_{j,v}\Sigma|j,\Sigma\rangle, \tag{9}$$

where ζ_{e} represents a purely electronic reduction factor and $d_{j,v}$ is the reduction factor of the spin-orbit interaction induced by the Jahn-Teller effect. The magnitude of $d_{j,v}$ depends on the vibronic state under consideration. For a weak linear Jahn-Teller interaction in one mode ($D << 1$), $d_{j,v}$ can be estimated using the relation [33]

$$d_{j,v} = \mp 1 \pm 4D(v+1) \quad \text{for } j = \ell_v \mp \frac{1}{2}. \tag{10}$$

Figure 1 illustrates the dependence of the energies of individual spin-vibronic states on the magnitude of the spin-orbit interaction ($a\zeta_{e}$) and on the strength of the linear Jahn-Teller coupling in one mode (D) calculated using Eqs. (3)-(7). The range of the coupling strengths of both interactions was chosen so that the situation encountered in the $\tilde{X}^{+}$ ^{2}E state of CH_3Cl^+ for the active mode ν_6 corresponds to the dashed vertical line in Fig. 1, with $D = D_6 = 0.009$. The spin-vibronic states in Fig. 1 are designated as sums of the basis states $|j, \ell_v, \Lambda, \Sigma\rangle$. Indeed, each spin-vibronic state is a superposition of a dominant contribution with a projection of the electronic angular momentum of $\Lambda = \pm 1$ and a weaker contribution (label in parentheses in Fig. 1) with $\Lambda = \mp 1$, each in combination with the value of ℓ_v satisfying Eq. (8) [31]. Because the projection of the electron spin onto the molecular z-axis (quantum number Σ) is not affected

by the Jahn-Teller interaction, its value is the same for both components of each spin-vibronic state. The basis states are conveniently labeled by the projection quantum number

$$\Omega' = \Lambda - \ell_v + \Sigma, \tag{11}$$

as explained in Ref. [4].

In the correlation diagram of Fig. 1, the situation corresponding to the ^{2}E ground state of CH$_3$Cl$^+$ is reached in two ways. On the left-hand side, it is reached by first increasing the spin-orbit-coupling strength $a\zeta_e$ from 0 to -645 cm$^{-1} \cdot 0.35 = -225.75$ cm^{-1} at $D = 0$ and then varying D from 0 to 0.009. On the right-hand side, it is reached by first varying D from 0 to 0.02 at $a\zeta_e = 0$, then increasing the spin-orbit-coupling strength $a\zeta_e$ from 0 to -225.75 cm^{-1}, and finally reducing D from 0.02 to 0.009. The spin-orbit interaction leads to the dominant splittings of both the 6^0 and 6^1 levels. The linear E $\otimes$ e Jahn-Teller effect induces an additional splitting of the vibrational levels into $v + 1$ components, and stabilizes each state in energy. The observable spin-orbit splitting $a\zeta_e d_{j,v}$ in the presence of a nonzero Jahn-Teller interaction is always reduced compared to the situation one would observe in the absence of Jahn-Teller coupling, in which case $|d_{j,v}| = 1$.

3.2 Rotational fine structure and photoionization selection rules

In the first part of this article series [4], the effective spin-rotational Hamiltonian $\hat{H}_{\mathrm{RSO}}$ originally derived by Brown [34]

$$
\begin{align}
\frac{\hbar^2}{hc}\hat{H}_{\mathrm{RSO}} \quad = \quad & B\hat{\vec{J}}^{\,2} + (A - B)\,\hat{J}_z^2 \tag{12a}\\
& -2A\hat{J}_z\hat{\pi}_z + A\hat{\pi}_z^2 \tag{12b}\\
& -2A\hat{J}_z\hat{S}_z + 2A\hat{S}_z\hat{\pi}_z + B\hat{\vec{S}}^{\,2} + (A - B)\,\hat{S}_z^2 + a\hat{L}_z\hat{S}_z \tag{12c}\\
& -B\left(\hat{J}_+\hat{S}_- + \hat{J}_-\hat{S}_+\right) \tag{12d}
\end{align}
$$

was used to calculate the rotational fine structure of the PFI-ZEKE photoelectron spectra of the $^2E_{3/2}$ ground states of CH_3I^+ and CD_3I^+. Equations (12a)-(12c) have the eigenvalues

$$\frac{E_{\mathrm{RSO}}}{hc} = BJ(J+1) + (A-B)P^2 \tag{13a}$$

$$- 2AP\zeta_{\mathrm{ev}} + A\zeta_{\mathrm{ev}}^2 \tag{13b}$$

$$- 2AP\Sigma + 2A\Sigma\zeta_{\mathrm{ev}} + \frac{B}{2} + \frac{A}{4} + a\zeta_{\mathrm{e}}d_{j,v}\Sigma. \tag{13c}$$

In Eq. (13), P represents the quantum number associated with the projection of $\vec{J}$ onto the molecular z axis. In calculations of the spin-rovibronic structure, the effects of the spin-uncoupling term (Eq. (12d)), which is not diagonal in the basis $|j, \Sigma, J, P\rangle$, must be included.

An interesting property of Hund's-case-(a)-coupled prolate-symmetric-top cations subject to the combined effects of Jahn-Teller and spin-orbit interactions, such as CH_3I^+ and CH_3Cl^+, is the existence of rotational satellite bands in the photoelectron spectrum [4, 16]. These satellite bands, observed in the PFI-ZEKE and MATI spectra of methyl iodide at low resolution by Kim and coworkers [16] and high resolution in Ref. [4], proved crucial for the understanding of the photoionization dynamics in such molecules, and led to the derivation of the rovibronic photoionization selection rules $\Delta P = \Omega' = \pm 3/2$ for transitions to the $^2E_{3/2}$ spin-orbit component of the ground state of CH_3I^+. The dominant contribution, $\Delta P = \Omega'_a = +3/2$, corresponds to the main component $|1/2, 0, 1, +1/2\rangle$ ($|\Omega'_a = +3/2\rangle$) of the spin-vibronic ground state. The weak satellite bands obey the selection rule $\Delta P = \Omega'_b = -3/2$, which originates from the weaker component ($|1/2, 1, -1, +1/2\rangle$) ($|\Omega'_b = -3/2\rangle$) of the ionic ground state wave function [4] (see Fig. 1).

The PFI-ZEKE photoelectron spectrum of the $\tilde{X}^+ \, ^2E \leftarrow \tilde{X} \, ^1A_1$ photoionizing transition of CH_3Cl can be analyzed in an analogous manner. For each spin-vibronic state, the quantum number Ω' describing the projection of the total spin-vibronic angular momentum onto the molecular z-axis [4, 9] can be directly determined from the two components of the wavefunctions $|j, \ell_v, \Lambda, \Sigma\rangle$ given in Fig. 1. We use the labels $|\Omega'_a\rangle$ and $|\Omega'_b\rangle$ to designate the dominant and the

minor components of the spin-vibronic states, respectively. The quantum number Ω' also allows the determination of the symmetry of the corresponding states in the spin double group $C_{3v}^2(M)$, because states with $\Omega' = 3n \pm 3/2$ and $\Omega' = 3n \pm 1/2$ (n integer) transform as the $E_{3/2}$ and $E_{1/2}$ irreducible representations, respectively [9].

In the partially rotationally resolved PFI-ZEKE photoelectron spectra of the ^2E ground state of CH_3Cl^+ presented in Section 4, the strongest rotational branches of each spin-vibronic band obey the photoionization selection rule $\Delta P = \Omega'_a$. The weaker satellite bands, which originate from $\Delta P = \Omega'_b$ rovibronic transitions, are more difficult to observe than in the spectrum of CH_3I^+, mainly because the effective vibronic Coriolis coupling [34, 35]

$$\hat{\pi}_z|j\rangle = \left(\zeta_{i_1,i_2} j + \zeta_e d_{j,v} - \frac{1}{2}\zeta_{i_1,i_2} d_{j,v} + \sum_{i'} \zeta_{i'_1,i'_2} \ell_{v_{i'}} \right) |j\rangle = \zeta_{ev}|j\rangle \tag{14}$$

is weaker in CH_3Cl^+ than in CH_3I^+.

In the analysis of the PFI-ZEKE photoelectron spectra of the $\tilde{X}^+\,^2E \leftarrow \tilde{X}\,^1A_1$ transition of CH_3Cl presented in the following section, the spin-vibronic eigenvalues were calculated using Eqs. (3)-(7) considering only one active Jahn-Teller vibration (ν_6). The rotational fine structure of the two spin-orbit components of each Jahn-Teller eigenstate was determined with Eqs. (12a)-(12d). The allowed rovibronic transitions were obtained by applying the selection rule $\Delta P = \Omega'$ discussed above and the general rovibronic symmetry selection rules [36] summarized in Table 4 of the first article of this series [4]. The contributions from the Coriolis coupling $\zeta_{i'_1,i'_2}$ of the degenerate e modes $i' \neq i$ ($i = 6$) were neglected in all calculations.

4 PFI-ZEKE photoelectron spectra and rovibronic analysis of the $\tilde{X}^+\,^2E \leftarrow \tilde{X}\,^1A_1$ transition of CH_3Cl at low energies

A survey of the PFI-ZEKE photoelectron spectrum of the $\tilde{X}^+\,^2E \leftarrow \tilde{X}\,^1A_1$ transition of CH_3Cl is presented in Fig. 2. The photoionization spectrum (grey trace) is also displayed to demonstrate that the first band of the PFI-ZEKE spectrum (black trace) corresponds to the adiabatic

ionization energy E_I of the $\tilde{X}^+$ $^2E \leftarrow \tilde{X}$ $^1A_1$ transition. Both naturally occurring isotopomers $CH_3^{35}Cl$ and $CH_3^{37}Cl$ contribute to the PFI-ZEKE photoelectron spectrum of CH_3Cl. The presence of two isotopomers, the weakness of most vibrational bands (apart from the $^2E_{3/2}$ origin band), and the spectral congestion made the spin-rovibronic analysis of the PFI-ZEKE photoelectron spectrum of CH_3Cl in the vicinity of the adiabatic ionization threshold challenging. In the following, we first discuss the spin-vibronic structure of the spectrum in Section 4.1, and then present the analysis of the partially resolved rotational structure of the vibrational bands in Section 4.2.

4.1   Assignment of the vibronic structure of the photoelectron spectrum of the $\tilde{X}^+$ $^2E \leftarrow \tilde{X}$ $^1A_1$ transition

The PFI-ZEKE photoelectron spectrum of CH_3Cl in the vicinity of the adiabatic ionization threshold consists of well-resolved vibronic bands appearing in pairs of lines separated by ~ 200 cm^{-1} (see Fig. 2). We attribute this splitting as arising from the spin-orbit coupling. The value of the Jahn-Teller quantum number $j = \ell_v + \frac{1}{2}\Lambda$ of the spin-vibronic states of the CH_3Cl^+ cation is indicated along the assignment bar in Fig. 2.

The origin band (0_0^0), with its two spin-orbit components at ~ 91060 cm^{-1} and ~ 91280 cm^{-1}, is the most intense, but weaker transitions to the first excited levels of four vibrational modes of the cation are also observed. They are labeled 2_0^1, 3_0^1, 5_0^1, and 6_0^1 in Fig. 2 and were assigned on the basis of calculations of the vibronic and rotational structure following the procedure described in Section 3. The 3_0^1 band, corresponding to the excitation of the totally-symmetric (a_1) C$-$Cl stretching mode, is the strongest, followed by the Jahn-Teller-active H_3C-Cl bending (e) mode (6_0^1), the totally-symmetric (a_1) umbrella mode (2_0^1), and the CH_3-deformation (e) mode (5_0^1). The intensity of the transitions to the lower spin-orbit component of most vibronic states of the cation is stronger than to the upper one by a factor of about two.

The main signatures of the $E \otimes e$ Jahn-Teller effect in CH_3Cl^+ are (1) the observation of

transitions to the first excited vibrational levels of the e modes ν_5 and ν_6, and (2) the fact that the $v_6 = 1$ level of ν_6 is split into four components by the spin-orbit and Jahn-Teller interactions (see also Fig. 1). In the absence of vibronic coupling, only transitions to totally-symmetric vibrational levels are allowed by symmetry. Distortion of the molecular structure along the Jahn-Teller-active (e) modes relaxes this selection rule, which makes photoelectron spectroscopy ideally suited to study the Jahn-Teller effect.

Consideration of Fig. 2 leads to the following qualitative conclusions: Jahn-Teller activity is observable along the two e modes ν_5 and ν_6, but is stronger along ν_6 than along ν_5. Indeed, the integrated intensity of the 6_0^1 band is more than five times larger than that of the 5_0^1 band, the assignment of which is tentative (see also below). Moreover, the splitting of each spin-orbit component into two Jahn-Teller-split components is clearly observable only in the 6_0^1 band. These conclusions justify, at least in the low energy region of the spectrum, the approximate single-mode treatment of the $E \otimes e$ Jahn-Teller effect in CH_3Cl^+ introduced in Section 3 and based on Eqs. (3)-(7).

The positions and assignments of the bands observed in Fig. 2 are summarized in Table 1. The origins of the bands were determined from their rotational structure with an absolute accuracy of better than 10 cm^{-1}, as explained in Section 4.2, except the two spin-orbit components of 5_0^1, which are too weak for an analysis of their rotational structure to be carried out. The second column of Table 1 lists the band origins calculated using Eqs. (3)-(7) after optimizing the linear Jahn-Teller coupling constant D_6 and the spin-orbit coupling constants $a\zeta_e d_{j=1/2,v=0}$, $a\zeta_e d_{j=3/2,v=1}$, and $a\zeta_e d_{j=1/2,v=1}$ (see Eq. (9)). The fundamental wave numbers of the experimentally observed vibrational modes, and the Jahn-Teller and spin-orbit-coupling parameters derived from the spin-vibronic analysis of the $\tilde{X}^{+2}E$ ground state of CH_3Cl^+ are summarized in Table 2, where they are compared to parameters determined in earlier spectroscopic studies. Overall, our analysis agrees best with that carried out by Karlsson *et al.* [1]. However, our value of the ν_6 harmonic wave number (1059.5(5.0) cm^{-1}) is significantly larger than the fundamen-

14

tal wave number reported in Ref. [1] for the two spin-orbit components of ν_6. Our vibrational wave numbers are larger than those reported by Locht *et al.* [8], and our assignments of the spin-orbit structure differs markedly from that proposed by Ragle *et al.* [5]. We believe that these discrepancies result from our ability to better resolve the spin-vibronic fine structure, and therefore obtain more information on the Jahn-Teller interaction strength than was possible in these earlier studies by threshold and He I photoelectron spectroscopy. We also note a satis-factory agreement between the fundamental wave numbers derived from our spectrum and the positions of the bands (some of which unassigned) observed in infrared spectra of CH_3Cl^+ in a neon matrix [7].

4.2 Analysis of the partially resolved rotational structures of the photoelec-tron spectrum of the $\tilde{X}^+ \, ^2E \leftarrow \tilde{X} \, ^1A_1$ transition of CH_3Cl

The assignment of the lowest spin-vibronic states of the ^2E ground state of CH_3Cl^+ presented in Section 4.1 is to a large extent based on the calculations of the rotational structure of the individual bands described in this section. Because of the previously discussed weak signal intensity in most PFI-ZEKE spectra presented here, each spin-vibronic band was assigned on the basis of its overall rotational contour, which allowed us to draw conclusions on the symmetry and the $\Delta P = P^+ - K$ subband structure. In the calculations of the rotational structure, the parameters that could not be adjusted reliably because of the weakness of the relevant spectral features (i.e., the rotational constants A^+ and B^+ of the excited vibrational levels and the relative intensities of individual ΔJ branches in the corresponding photoelectron spectra) were kept as determined for the origin bands, the intensities of which are strong enough to allow the determination of a reliable set of parameters.

To account for the contributions of the $CH_3^{37}Cl$ isotopomer to the experimental spectra, we estimated the isotopic shifts of the different bands from spectroscopic data available on the $\tilde{X} \, ^1A_1$ ground state [37] and from the vibrational wave numbers of $CH_3^{35}Cl^+$ from the spin-vibronic

analysis presented in Section 4.1 (see Table 2). From the harmonic vibrational wave numbers in the $\tilde{X}\,^1A_1$ ground state of $CH_3^{35}Cl$ and $CH_3^{37}Cl$ [37], we estimate that the differences in zero-point energies of the two neutral isotopomers $ZPE(CH_3^{35}Cl)-ZPE(CH_3^{37}Cl)$ is ~ 3.8 cm^{-1}. From the vibrational intervals we measured in the cation for ν_2, ν_3, ν_5 and ν_6, and if we assume that the C$-$H stretching (ν_1 and ν_4) vibrational frequencies do not appreciably change upon ionization and that the isotopic substitution hardly affects these frequencies, we estimate the differences of the zero-point energy of the two cationic isotopomers $(ZPE(CH_3^{35}Cl^+)-ZPE(CH_3^{37}Cl^+))$ of CH_3Cl^+ in the $\tilde{X}^{+2}E$ ground state to be ~ 3.4 cm^{-1}. Therefore, the isotopic shift of the adiabatic ionization energy $E_I(CH_3^{35}Cl^+) - E_I(CH_3^{37}Cl^+)$ is estimated to be ~ -0.4 cm^{-1} with an uncertainty of ~ 3 cm^{-1}. The only significant isotopic shift expected for the bands measured in the present study concerns the 3_0^1 band, for which we estimate an isotopic shift of ~ 5.1 cm^{-1}. Consequently, we have assumed in the calculations of the rotational structures presented in this section that the origin band of $CH_3^{37}Cl$ is shifted by 0.4 cm^{-1} with respect to the corresponding band of $CH_3^{35}Cl$, the 2_0^1 band by 0.2 cm^{-1}, the 5_0^1 band by 0.4 cm^{-1}, the 6_0^1 band by 0.0 cm^{-1}, and the 3_0^1 band by -4.7 cm^{-1}.

The rotational structure of the 0_0^0 origin band

The PFI-ZEKE photoelectron spectra of the $\tilde{X}^+\,^2E_\Omega$ ($\Omega = \frac{1}{2}, \frac{3}{2}$) $\leftarrow \tilde{X}\,^1A_1$ photoionizing transition recorded at a resolution of 0.6 cm^{-1} ($\Omega = \frac{3}{2}$ component) and 1.0 cm^{-1} ($\Omega = \frac{1}{2}$ component) are displayed in the top panels of Fig. 3. The rotational structure of these spectra could only be partially resolved because of the high density of rotational lines and the overlap of the spectra of $CH_3^{35}Cl$ and $CH_3^{37}Cl$.

To extract molecular parameters from these congested spectra, an iterative procedure was followed. The population of the ground state level was assumed to be described by a Boltzmann distribution and the intensity of transitions from different rotational levels in the neutral molecule were weighted proportionally to their statistical weights (i.e., 16 and 16 for levels of A and E

rovibronic symmetry, respectively [38]). The values of the rotational constants of the ground state of CH$_3^{35}$Cl ($A = 156052.050(47)$ MHz, $B = 13292.87681(10)$ MHz) and of CH$_3^{37}$Cl ($A = 156053.187(38)$ MHz, $B = 13088.171261(71)$ MHz) were taken from Refs. [39, 40]. Allowed transitions were determined using the angular momentum conservation rule [41]

$$\Delta J = -\ell - 3/2, -\ell - 1/2, ..., \ell + 3/2, \tag{15}$$

where ℓ represents the orbital angular momentum quantum number of the photoelectron partial wave, and the photoionization selection rule appropriate for Hund's-case-(a)-type angular momentum coupling in the cation [4]

$$\Delta P = \Omega', \tag{16}$$

with $\Omega' = \Omega'_a$ for the main branches and $\Omega' = \Omega'_b$ for the subbands, as explained in Section 3.2. Starting from initial guesses of the rotational temperature in the supersonic jet, the rotational constants A^+ and B^+, the Coriolis coupling constant $A^+\zeta_{ev}$, and of the relative intensities of the different rotational branches, these parameters were systematically adjusted until the calculated spectrum best matched the experimental spectrum. We found a temperature $T_{rot} = 12$ K and intensity ratios $(|\Delta J| = 1/2) : (|\Delta J| = 3/2) : (|\Delta J| = 5/2) : (|\Delta J| = 7/2)$ of $1 : 0.6 : 0.4 : 0.2$ and $(\Delta P = \Omega'_a) : (\Delta P = \Omega'_b)$ of $5 : 1$ for the different branches to best reproduce the measured intensities. The observation of the $\Delta P = -3/2$ subband in the spectrum of the $\tilde{X}^+$ $^2E_{3/2} \leftarrow \tilde{X}$ $^1A_1$ transition and of the $\Delta P = -5/2$ subband in that of the $\tilde{X}^+$ $^2E_{1/2} \leftarrow \tilde{X}$ $^1A_1$ transition (see dashed vertical lines in Fig. 3) enabled the determination of $A^+\zeta_{ev}$, although the weakness of these subbands and the partial overlap with the main bands (composed of $\Delta P = +3/2$ and $\Delta P = +1/2$ transitions for the $^2E_{3/2}$ and $^2E_{1/2}$ components, respectively) resulted in large uncertainties.

The values of the band centers and rotational constants derived from this analysis are presented in Tables 1 and 3, respectively. The calculated spectra are displayed in Fig. 3 as stick

17

spectra (lower panels) and spectra convoluted with a Gaussian line-shape function (middle panels) with a full-width-at-half-maximum of 0.6 cm^{-1} and 1.0 cm^{-1} for the $^2E_{3/2}$ and $^2E_{1/2}$ spin-orbit components, respectively. The contributions of $CH_3^{37}Cl$ to these spectra are indicated in grey.

Rotational structure of the 2_0^1 and 3_0^1 bands

An enlarged view of the PFI-ZEKE photoelectron spectrum of the $\tilde{X}^+\ ^2E \leftarrow \tilde{X}\ ^1A_1\ 3_0^1$ transition of CH_3Cl is presented in the top panel of Fig. 4. From the similarity of the band shapes of the two spin-orbit components and the two components of the origin bands presented in Fig. 3, one readily concludes that they correspond to totally-symmetric vibrational bands. The calculations of the rotational structure of these bands were therefore carried out in the same way as those of the origin bands and are shown as stick spectra in the bottom panels of Figure 4, and after convolution with Gaussian line-shape functions ($\Gamma_{FWHM} = 1$ cm^{-1}) in the middle panels for direct comparison to the experimental spectra. The main difference to the structure of the origin band is the larger spin-orbit splitting observed in the 3_0^1 band, $-241.9(5.0)$ cm^{-1} compared to the ground-state splitting $a\zeta_e d_{j=1/2,v=0} = -217.5(2.0)$ cm^{-1}. This increase of the spin-orbit splitting was already observed by Karlsson and coworkers [1] (see Table 2), who determined individual vibrational frequencies for each spin-orbit component. The origin of this increased spin-orbit coupling in the 3_0^1 band of CH_3Cl^+ cannot be explained by our single-mode spin-vibronic model, and an effective spin-orbit-splitting parameter $a\zeta_e d_{j=1/2,v_3=1}$ was therefore used in the calculations. Nevertheless, the calculations of the rotational contour of the 3_0^1 band reproduce the experimental observations satisfactorily, and also correctly predict the energies of several of the subbands obeying the rovibronic selection rule $\Delta P = \Omega_b'$, as indicated by the dashed vertical lines in Fig. 4.

The top panel of Fig. 5 presents an enlarged view of the PFI-ZEKE photoelectron spectrum of the $\tilde{X}^+\ ^2E \leftarrow \tilde{X}\ ^1A_1$ transition of CH_3Cl of the region $1500 - 1900$ cm^{-1} above the adiabatic

ionization threshold. In this region, transitions to the first excited vibrational levels of the ν_2 and ν_5 modes of CH_3Cl^+ are expected. The two strongest features of this spectrum, at $\sim 92\,610$ cm^{-1} and $\sim 92\,830$ cm^{-1}, are assigned to transitions to the spin-orbit-split components of the 2_0^1 band, because the similarity of the band contour with the contours observed for the origin and the 3_0^1 band indicates a transition to a totally symmetric vibrational band.

The calculations of the rovibronic transitions were carried out in the same way as those of the 3_0^1 band and resulted in the determination of the band origin and spin-orbit splitting $a\zeta_e d_{j=1/2,v_2=1}$ listed in Table 2. The calculated spectra are displayed in Fig. 5 as stick spectra (bottom panel) and after convolution with a Gaussian lineshape of 1.0 cm^{-1} FWHM (middle panel). Given the weakness and the resulting poorer signal-to-noise ratio of the spectrum displayed in Fig. 5, the assignments must remain tentative and the molecular parameters have a large uncertainty.

The 5_0^1 and 6_0^1 bands and the Jahn-Teller effect along ν_6

Next to the two spin-orbit components of the 2_0^1 band, two additional very weak bands, marked by asterisks in Fig. 5, are observed in the PFI-ZEKE spectrum. As explained in Section 4.1, we tentatively assign them to transitions to the two spin-orbit components of the Jahn-Teller-active mode ν_5. The weakness of these experimental transitions prevented us from carrying out an analysis of their rovibronic structure, and the determined band centers (Table 2) have a large uncertainty.

The 6_0^1 band of the photoelectron spectrum of CH_3Cl represents the key to understand the Jahn-Teller effect in the $\tilde{X}^+$ ^2E ground state of CH_3Cl^+ at low energies. Compared to the other bands observed in Fig. 2, both spin-orbit components of the 6_0^1 band appear broader, and the overall structure is indicative of a further splitting of each spin-orbit component by the Jahn-Teller effect, resulting in the four spin-vibronic components labeled along the assignment bar of Fig. 2. Because of the partial overlap of the rotational structure of the spin-vibronic

19

components, the modeling of their rotational structure turned out to be essential to derive the Jahn-Teller coupling parameters.

The PFI-ZEKE photoelectron spectrum of the $\tilde{X}^+ \, ^2E \leftarrow \tilde{X} \, ^1A_1 \, 6_0^1$ transition is displayed on an enlarged scale in the top panel of Fig. 6, where it is compared with the calculated stick spectrum (bottom panel of Fig. 6) and a spectrum obtained after convolution of the stick spectrum with a Gaussian line-shape function with a full-width-at-half-maximum of 1.0 cm^{-1} (middle panel of Fig. 6). The analysis was based on separate calculations of (i) the rotational structure of the spectrum using Eqs. (12a)-(12d) in combination with the rotational constants B^+ and $A^+\zeta_{ev}$ and the branch intensity ratios derived from the analysis of the origin bands, and (ii) the spin-vibronic calculations based on Eqs. (3)-(7). The former calculations led to the determination of the band origins listed in Table 1, and the latter to the derivation of a set of Jahn-Teller coupling parameters ($D_6 = 0.009(1)$, $\omega_6 = 1059.5(8.0)$ cm^{-1} and $\zeta_e = 0.35(4)$) which best reproduce the band origins. When determining these parameters, the positions of the two spin-orbit components of the 0_0^0 transition and of the lowest two components of the 6_0^1 transition were given large statistical weights because of their stronger intensity.

Assuming that the spin-orbit coupling constant a is the same as in HCl$^+$ (i.e., $-645(5)$ cm^{-1} [42]), the calculated spin-orbit splittings $\Delta_{j,v}$

$$\Delta_{j=1/2,v=0} \;=\; -217.57 \text{ cm}^{-1} \tag{17}$$

$$\Delta_{j=3/2,v=1} \;=\; -210.27 \text{ cm}^{-1} \tag{18}$$

$$\Delta_{j=1/2,v=1} \;=\; +209.09 \text{ cm}^{-1} \tag{19}$$

can be used to determine the parameters $d_{j,v}$ as (see Eq. (9))

$$d_{j,v} = \Delta_{j,v}/(a\zeta_e). \tag{20}$$

The results ($d_{j=1/2,v=0} = 0.963(20)$; $d_{j=3/2,v=1} = 0.931(20)$; $d_{j=1/2,v=1} = -0.926(20)$) indicate that the spin-orbit coupling is only weakly reduced by the Jahn-Teller effect.

Equation (14) enables one to estimate the value of $\zeta_{ev}^{j,v}$ from those of ζ_e (= 0.35(4), see above) and $d_{j,v}$. The influence on $\zeta_{ev}^{j=1/2,v=0}$ of the terms involving the Coriolis coupling constant $\zeta_{6_1,6_2}^{j=1/2,v=0}$, which describes the Coriolis interaction between the two components 6_1 and 6_2 of the degenerate mode, is very small. Indeed, varying $\zeta_{6_1,6_2}^{j=1/2,v=0}$ over the entire range of physically meaningful values $[0,1]$ only changes $\zeta_{ev}^{j=1/2,v=0}$ over the range $[0.337, 0.356]$. From the value of $A^+ \zeta_{ev}^{j=1/2,v=0} = 1.95(5)$ cm^{-1} determined for the origin band, we conclude that $A^+ = 5.79(+0.06; -0.15)$ cm^{-1}. From the value of A^+ and the range of $A^+ \zeta_{ev}^{j,v=1}$ values compatible with the measured spectra of the 6_0^1 band, we can further estimate that $\zeta_{ev}^{j=3/2,v=1}$ and $\zeta_{ev}^{j=1/2,v=1}$ must lie in the ranges $[0.32, 0.74]$ and $[-0.33, 0.07]$, respectively, which in turn implies that the value of $\zeta_{6_1,6_2}^{j,v=1}$ must be in the range $[0, 0.4]$.

5 Conclusions

Although the present study of the photoelectron spectrum of CH_3Cl did not provide full resolution of the rotational structure, the observation and analysis of the partially resolved rotational structure of several well-resolved spin-vibronic bands has permitted an improved characterization of the Jahn-Teller effect along the H_3C-Cl bending mode ν_6 in the $\tilde{X}^+$ ^2E ground state of CH_3Cl^+ at low energies. The Jahn-Teller effect is weak and dominated by the linear coupling term. The rotational structure does not provide evidence for a static distortion of the molecular structure from C_{3v} to C_s symmetry. Instead, the photoelectron spectra are characteristic of a dynamical Jahn-Teller effect and the rotational subband structure and rovibronic photoionization selection rules can be described satisfactorily in the $C_{3v}^2(M)$ spin double group. In particular, the rovibronic photoionization selection rule $\Delta P = \Omega' = \Lambda - \ell_v + \Sigma$ derived in our previous analysis of the rotational structure of the origin band of the photoelectron spectrum of CH_3I [4] was found to also be valid in CH_3Cl and applicable to bands associated with excited spin-vibronic levels of CH_3Cl^+.

In CH_3I^+, the Jahn-Teller effect is almost entirely masked by the strong spin-orbit coupling

and primarily detectable through weak rotational subbands in the photoelectron spectra that are forbidden in the absence of vibronic coupling [4]. In CH_3Cl^+, the spin-orbit interaction is much reduced, which facilitates the observation of the Jahn-Teller effect through the spin-vibronic band structure and also through the reduction of the spin-orbit coupling. Whereas the spin-orbit splitting of the X^+ $^2\Pi$ ground state of HCl^+ [42] indicates an atomic-like [43] spin-orbit coupling constant a in the range $585 - 650$ cm^{-1}, the effective spin-orbit coupling $a\zeta_e d$ is much reduced (to ~ 200 cm^{-1}, i.e., $\zeta_e d = 0.34$) in the $\tilde{X}^+$ ^2E ground state of CH_3Cl^+, by two effects. The dominant one is a purely electronic effect and can be described by the reduction factor $\zeta_e = 0.35(4)$ originating from a partial transfer of the spin-density to the methyl group [44]. The minor effect in the reduction results from the Jahn-Teller effect ($d \approx 0.96$). These effects are more pronounced than in the $\tilde{X}^+$ ^2E ground state of CH_3I^+ ([$0.97 \leq \zeta_e \leq 1$], [$0.95 \leq d < 1$]) and the $\tilde{X}$ ^2E ground state of the isoelectronic molecule CH_3S ($\zeta_e d \approx 0.68$ [9]). These differences, which are surprising at first sight, can be qualitatively accounted for by a simple model of the electronic structure, as will be explained in the last part of this article series [44].

The main merits of the single-mode treatment of the linear Jahn-Teller effect used in the analysis of the photoelectron spectrum of CH_3Cl are its simplicity and its ability to explain the experimental observation in a qualitatively satisfactory manner. To reach a complete and quantitatively accurate description of the Jahn-Teller effect in CH_3Cl^+, it would be desirable to also include quadratic couplings, and the pseudo-Jahn-Teller effect that arises from the interaction with the third component of the effective P state, i.e., the $\tilde{A}^+$ $^2A_1$ $(\sigma_{C-Cl})^{-1}$ electronic state, and to include all modes and all anharmonic couplings, as has been done for CH_3F^+ in prospective calculations [27, 28]. In the case of CH_3Cl^+, these extensions could then be tested by their ability to explain the observed mode-specific variation of the spin-orbit splittings (see Table 2) and the relative intensities of the different bands. Experimentally, more could be gained from the full resolution of the rotational structure. Although the experimental methods to achieve this goal are available (see Refs. [25, 45]) and were used in our study of CH_3I [4], they require an

intense source of narrow-band VUV radiation tunable in the range $90000 - 95000$ cm^{-1}, which is not available to us yet, or resonant multi-photon excitation schemes as exploited in Ref. [20].

Acknowledgements

References

[1] L. Karlsson, R. Jadrny, L. Mattsson, F.T. Chau and K. Siegbahn, Physica Scripta **16**, 225 (1977).

[2] F.T. Chau and L. Karlsson, Physica Scripta **16**, 258 (1977).

[3] W. Domcke, D.R. Yarkony and H. Köppel, editors, *Conical intersections: Electronic structure, dynamics and spectroscopy* Adv. Ser. in Phys. Chem., Vol. 15 (World Scientific Publishing Co., Singapore, 2004).

[4] M. Grütter, J.M. Michaud and F. Merkt, J. Chem. Phys. **134**, 054308 (2011).

[5] J.L. Ragle, I.A. Stenhouse, D.C. Frost and C.A. McDowell, J. Chem. Phys. **53**, 178 (1970).

[6] R.N. Dixon, J.N. Murrell and B. Narayan, Mol. Phys. **20**, 611 (1971).

[7] C.L. Lugez, D. Forney, M.E. Jacox and K.K. Irikura, J. Chem. Phys. **106** (2), 489 (1996).

[8] R. Locht, B. Leyh, A. Hoxha, D. Dehareng, K. Hottmann, H.W. Jochims and H. Baumgärtel, Chem. Phys. **272**, 293 (2001).

[9] T.A. Barckholtz and T.A. Miller, Int. Rev. Phys. Chem. **17** (4), 435 (1998).

[10] Y. Endo, S. Saito and E. Hirota, J. Chem. Phys. **81**, 122 (1984).

[11] D. Melnik, J. Liu, R.F. Curl and T.A. Miller, Mol. Phys. **105**, 529 (2007).

[12] Y. Endo, S. Saito and E. Hirota, J. Chem. Phys. **85**, 1770 (1986).

[13] M. Grütter, X. Qian and F. Merkt, unpublished results (2011).

[14] X. Xing, P. Wang, B. Reed, S.J. Baek, and C.Y. Ng, J. Phys. Chem. A **112**, 9277 (2008).

[15] M. Lee and M.S. Kim, J. Chem. Phys. **127**, 124313 (2007).

[16] M. Lee, Y.J. Bae and M.S. Kim, J. Chem. Phys. **128**, 044310 (2008).

[17] Y.J. Bae and M.S. Kim, J. Chem. Phys. **128**, 124324 (2008).

[18] Y.J. Bae and M.S. Kim, ChemPhysChem **9**, 1709 (2008).

[19] P. Wang, X. Xing, K.C. Lau, H.K. Woo and C.Y. Ng, J. Chem. Phys. **121**, 7049 (2004).

[20] X. Xing, B. Reed, M.K. Bahng, S.J. Baek, P. Wang and C.Y. Ng, J. Chem. Phys. **128**, 104306 (2008).

[21] R. Locht, B. Leyh, A. Hoxha, H.W. Jochims and H. Baumgärtel, Chem. Phys. **272**, 259 (2001).

[22] S. Eden, P. Limao-Vieira, S.V. Hoffmann and N.J. Mason, Chem. Phys. **331**, 232 (2007).

[23] P. Rupper and F. Merkt, Rev. Sci. Instrum. **75** (3), 613 (2004).

[24] F.M. Phelps III, editor, *M.I.T. Wavelength Tables*, Vol. 2, Wavelengths by Element (MIT Press, Cambridge, MA, 1982).

[25] U. Hollenstein, R. Seiler, H. Schmutz, M. Andrist and F. Merkt, J. Chem. Phys. **115** (12), 5461 (2001).

[26] I.B. Bersuker, *The Jahn-Teller effect* (Cambridge University Press, Cambridge UK, 2006).

[27] S. Mahapatra, V. Vallet, C. Woywood, H. Köppel and W. Domcke, Chem. Phys. **304**, 17 (2004).

[28] S. Mahapatra, V. Vallet, C. Woywood, H. Köppel and W. Domcke, J. Chem. Phys. **123**, 231103 (2005).

[29] B.F. Yates, W.J. Bouma and L. Radom, J. Am. Chem. Soc. **109**, 2250 (1987).

[30] J.W. Gauld and L. Radom, J. Phys. Chem. **98**, 777 (1994).

[31] H.C. Longuet-Higgins, U. Öpik, M.H.L. Pryce and R.A. Sack, Proc. R. Soc. London Ser. A **244** (1236), 1 (1958).

[32] H.A. Kramers, Proc. Kon. Akad. Wet. Amsterdam **33**, 959 (1930).

[33] M.S. Child, J. Mol. Spectrosc. **10**, 357 (1963).

[34] J.M. Brown, Mol. Phys. **20** (5), 817 (1971).

[35] M.S. Child and H.C. Longuet-Higgins, Phil. Trans. R. Soc. London Ser. A **254** (1041), 259 (1961).

[36] R. Signorell and F. Merkt, Mol. Phys. **92** (5), 793 (1997).

[37] A.V. Nikitin, J. Mol. Spectrosc. **252**, 17 (2008).

[38] G. Herzberg, *Molecular Spectra and Molecular Structure, Volume II, Infrared and Raman Spectra of Polyatomic Molecules* (Van Nostrand Reinhold Company, New York, 1945).

[39] L.N. Stříteská, M. Šimečková, P. Kania, P. Musil, L. Kolesniková, J. Koubek and Š. Urban, J. Mol. Struct. **919**, 89 (2009).

[40] A. Nikitin and J.P. Champion, J. Mol. Spectrosc. **230**, 168 (2005).

[41] J. Xie and R.N. Zare, J. Chem. Phys. **97** (5), 2891 (1992).

[42] A.W. Potts and W.C. Price, Trans. Farad. Soc. **67**, 1242 (1971).

[43] J.E. Sansonetti, W.C. Martin and S.L. Young, Handbook of Basic Atomic Spectroscopic Data (version 1.1.2) National Institute of Standards and Technology, Gaithersburg, MD, , [Online] http://physics.nist.gov/Handbook [2010, Nov 18] 2005.

[44] M. Grütter and F. Merkt, unpublished results (2011).

[45] F. Merkt, S. Willitsch and U. Hollenstein, High-resolution Photoelectron Spectroscopy, in *Handbook of High-Resolution Spectroscopy*, edited by M. Quack and F. Merkt, Vol. 3 (Wiley & Sons, Chichester, UK, 2011; ISBN 978-0-470-06653-9), ISBN 978-0-470-06653-9.
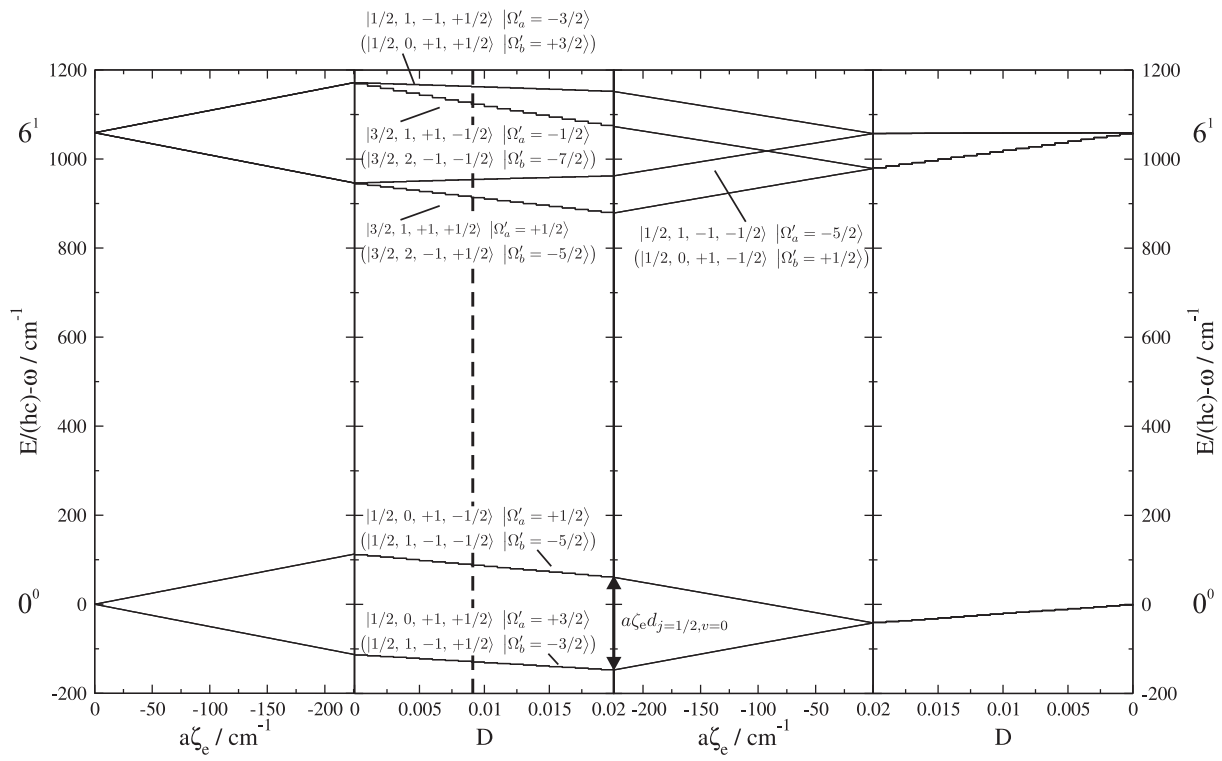
Figure 1: Internal energy level structure of the lowest spin-vibronic states of CH_3Cl^+ in dependence of the linear Jahn-Teller coupling strength in one mode (D) and the spin-orbit coupling ($a\zeta_e$). The dashed vertical line corresponds to the situation encountered in the mode ν_6 of the ^2E ground state of CH_3Cl^+ with the parameters taken from Table 2. The spin-vibronic states are sums of the basis states $|j, \ell_v, \Lambda, \Sigma\rangle$, and each level consists of a dominant $\Lambda = \pm1$ and a weaker $\Lambda = \mp1$ (in parentheses) contribution. Also indicated are the molecular-z-axis projections of the total angular momentum excluding rotation for the dominant ($|\Omega'_a\rangle$) and for the weaker ($|\Omega'_b\rangle$) contributions.
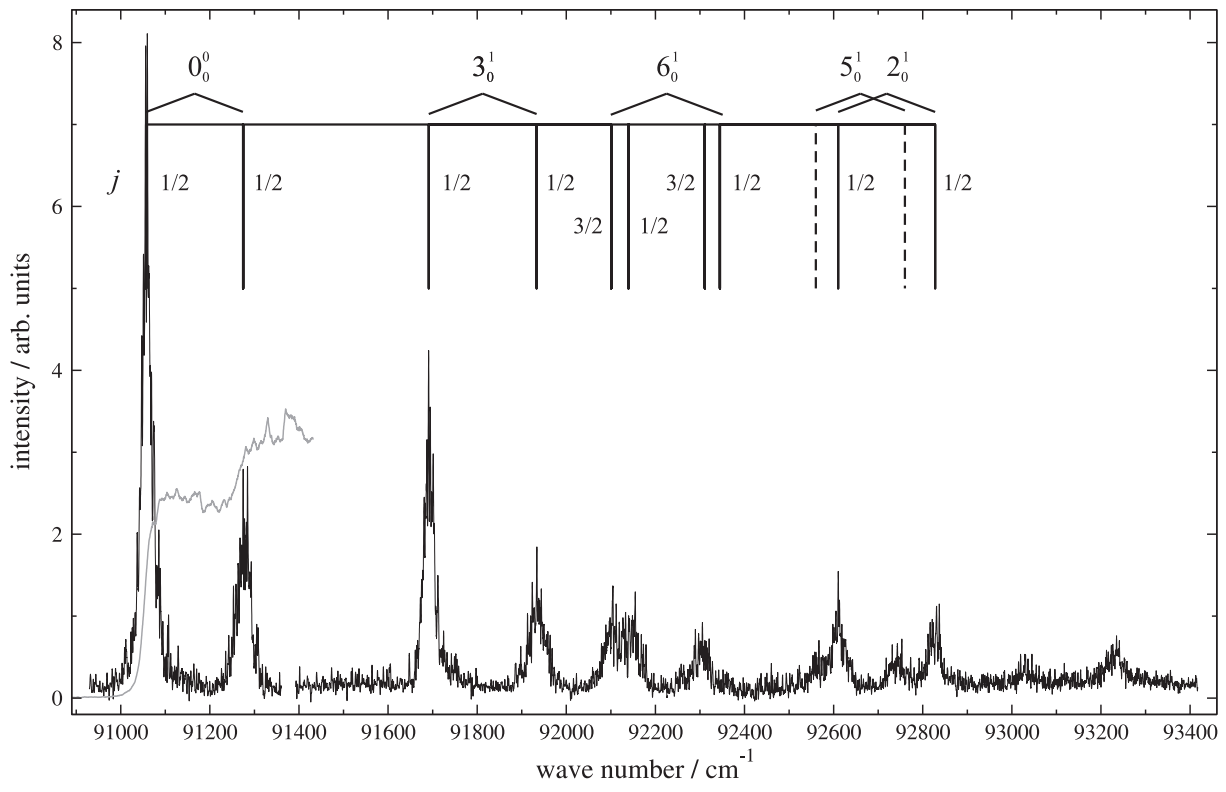
Figure 2: Overview of the PFI-ZEKE photoelectron spectrum of the $\tilde{X}^+\ ^2E \leftarrow \tilde{X}\ ^1A_1$ transition of CH_3Cl in the vicinity of the adiabatic ionization threshold. The assignment bars label the bands using the notation $\nu_{i0}^{v_i}$. The quantum number $j = \ell_v + \frac{1}{2}\Lambda$ of each assigned level is given below the assignment bar. The photoionization spectrum of CH_3Cl is displayed as a grey trace. The tentatively assigned spin-orbit-split band 5_0^1 is labeled by dashed vertical lines.
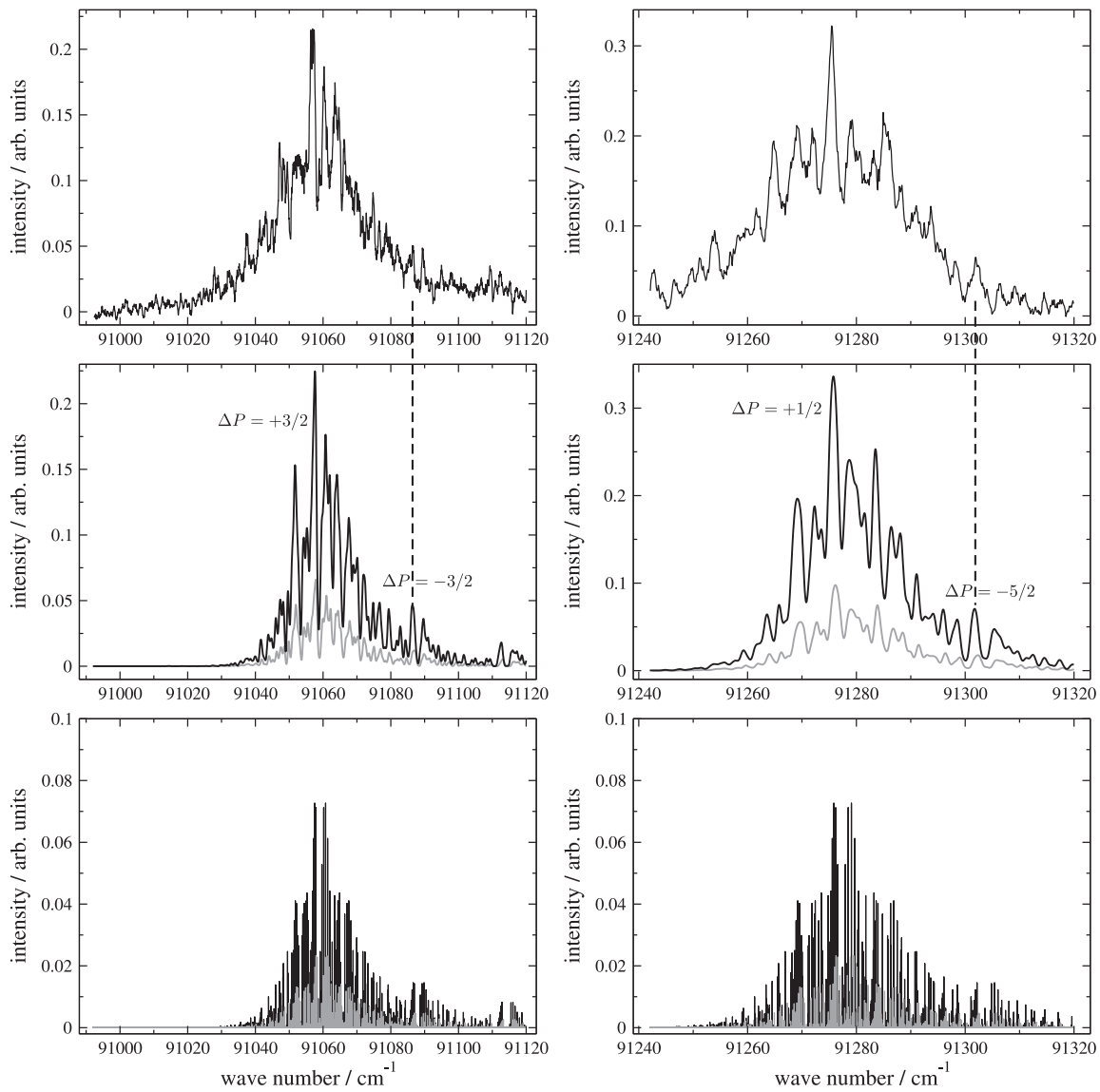
Figure 3: PFI-ZEKE photoelectron spectra of the two spin-orbit components of the origin band of the $\tilde{X}^+$ $^2E \leftarrow \tilde{X}$ $^1A_1$ ionizing transition of CH_3Cl. The left-hand-side and right-hand-side panels depict the transitions to the lower ($^2E_{3/2}$) and upper ($^2E_{1/2}$) components of the ionic ground state, respectively. The top, bottom and middle panels display the experimental spectra, calculated stick spectra and spectra obtained by convolution of the latter with a Gaussian line-shape function, respectively. The contributions to the $\tilde{X}^+$ $^2E \leftarrow \tilde{X}$ $^1A_1$ transition from $CH_3^{37}Cl$ are indicated in grey.

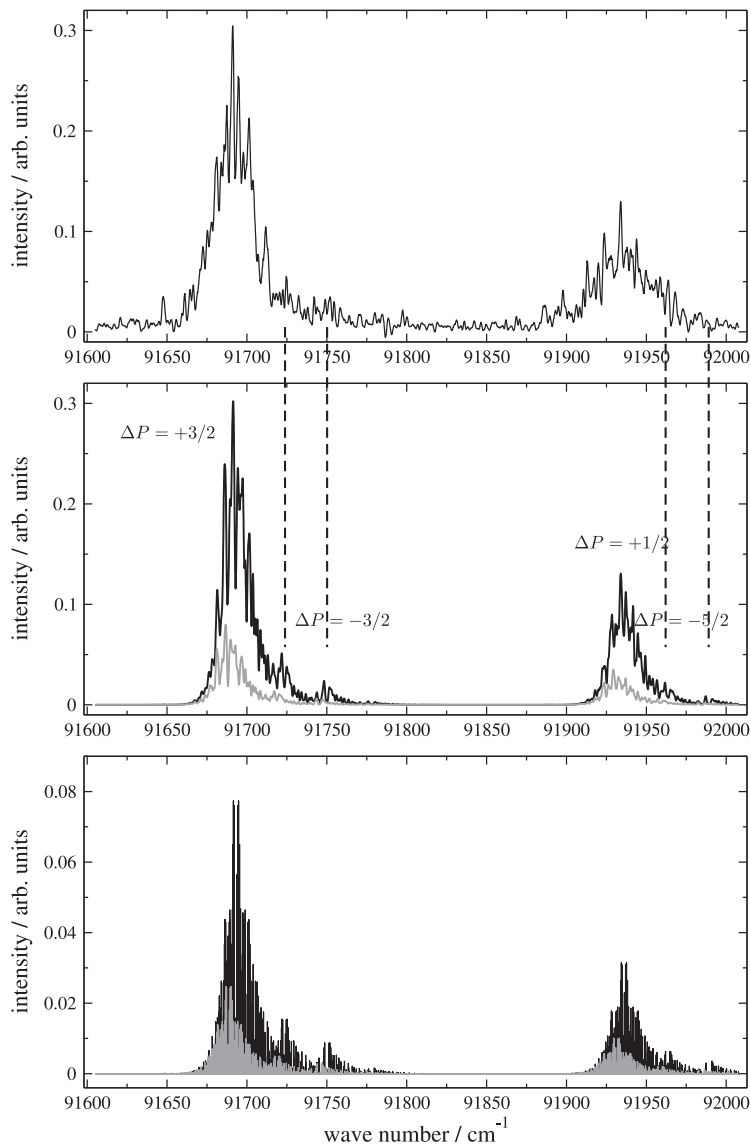Figure 4: Comparison of the PFI-ZEKE photoelectron spectrum of the $\tilde{X}^+$ $^2E \leftarrow \tilde{X}$ $^1A_1$ 3^1_0 transition of CH_3Cl (top panel) with a stick spectrum of the rotational structure calculated with the parameters from Table 3 (bottom panel). The middle panel shows a convolution of the stick spectra of $CH_3^{35}Cl$ and $CH_3^{37}Cl$ with a Gaussian line-shape function with a full-width-at-half-maximum of 1.0 cm^{-1} (black trace). The contributions from $CH_3^{37}Cl$ are indicated in grey.
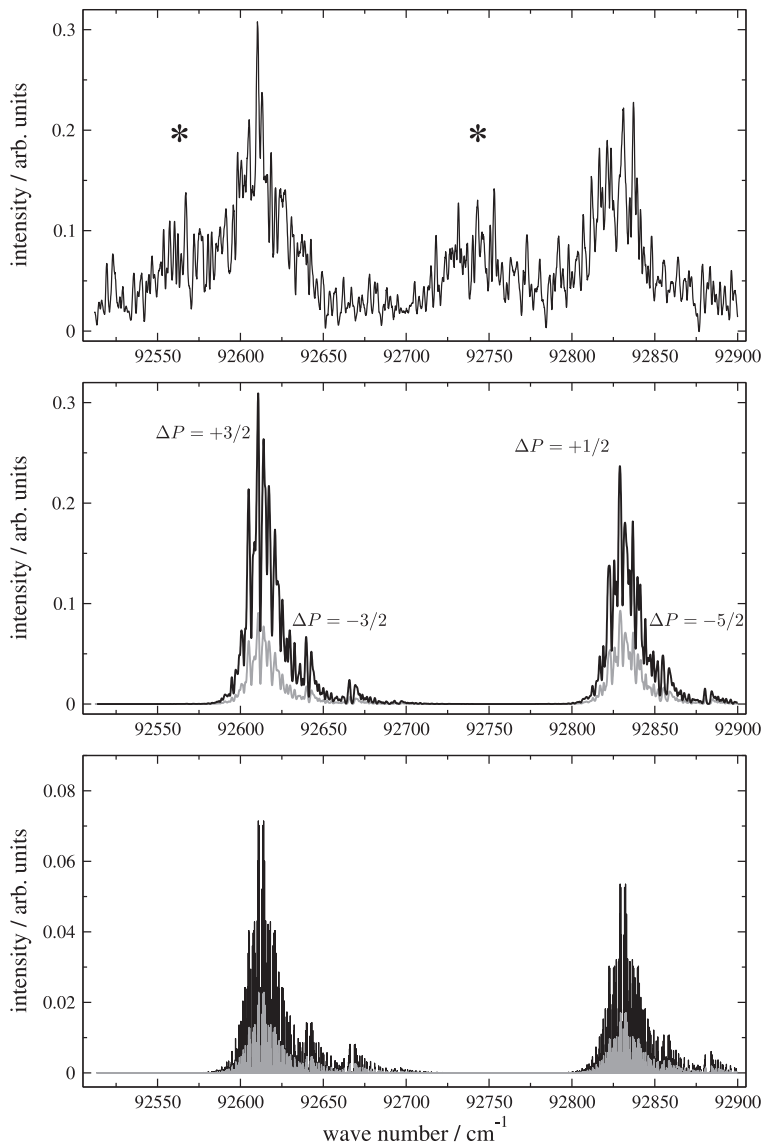
Figure 5: Comparison of the PFI-ZEKE photoelectron spectrum of the $\tilde{X}^+\ ^2E \leftarrow \tilde{X}\ ^1A_1\ 2_0^1$ transition of CH_3Cl (top panel) with a stick spectrum of the rotational structure calculated with the parameters from Table 3 (bottom panel). The middle panel shows a convolution of the stick spectrum with a Gaussian line-shape function with a full-width-at-half-maximum of $1.0\ cm^{-1}$. The additional spectral features marked by asterisks in the experimental spectrum (top panel) are tentatively assigned to the spin-orbit-split components of the 5_0^1 band. The contributions from $CH_3^{37}Cl$ are indicated in grey.

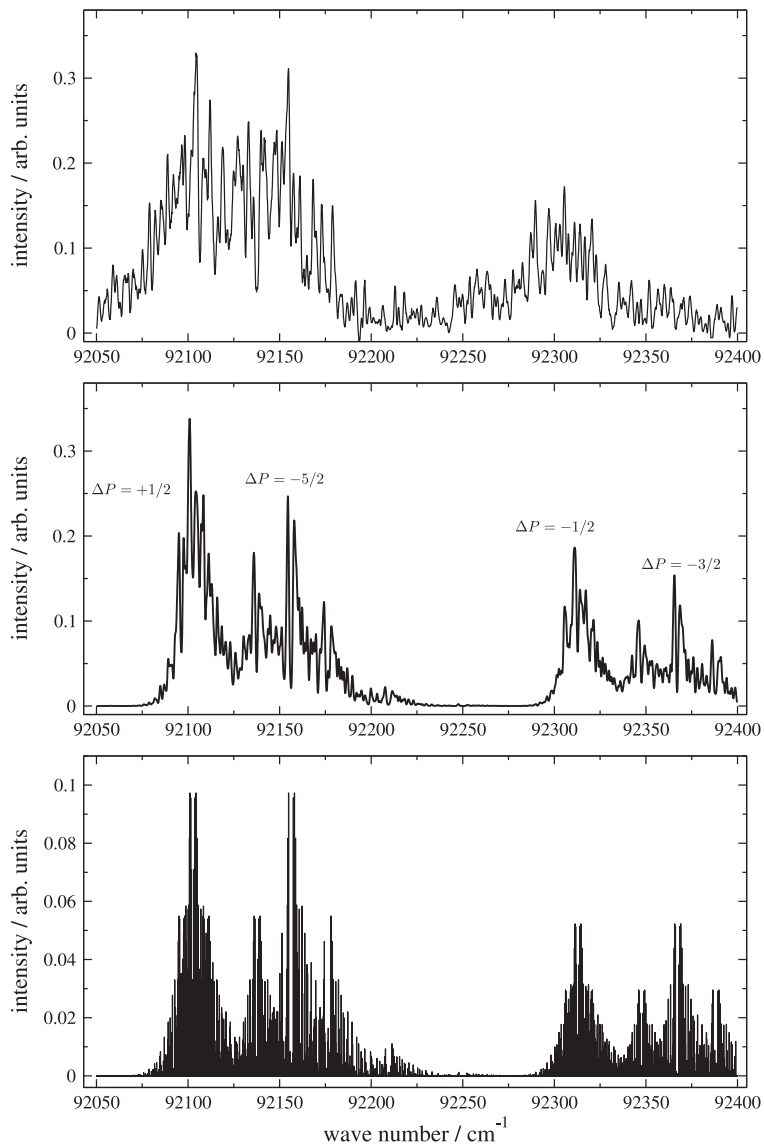Figure 6: Comparison of the PFI-ZEKE photoelectron spectrum of the $\tilde{X}^+$ $^2E \leftarrow \tilde{X}$ $^1A_1$ 6_0^1 transition of CH_3Cl (top panel) with a stick spectrum of the rotational structure calculated with the parameters from Table 3 (bottom panel), and the convolution of the latter with a Gaussian line-shape function with a full-width-at-half-maximum of 1.0 cm^{-1} (middle panel).

$\frac{E_{\text{exp}}}{hc}$ / cm^{-1}	$\frac{E_{\text{calc}}}{hc}$ / cm^{-1}	Assignment (Γ_{ves})
91057.0(2.0)	91057.0	0-0 ($E_{3/2}$)
91274.5(2.0)	91274.6	0-0 ($E_{1/2}$)
91692.3(5.0)		ν_3 ($E_{3/2}$)
91934.2(5.0)		ν_3 ($E_{1/2}$)
92101.5(5.0)	92101.2	ν_6 $j = 3/2$ ($E_{1/2}$)
92139.5(5.0)	92140.1	ν_6 $j = 1/2$ ($E_{1/2}$)
92311.7(5.0)	92311.5	ν_6 $j = 3/2$ ($E_{1/2}$)
92348.5(10.0)	92349.2	ν_6 $j = 1/2$ ($E_{3/2}$)
(92560)		ν_5
92611.2(5.0)		ν_2 ($E_{3/2}$)
(92740)		ν_5
92828.7(5.0)		ν_2 ($E_{1/2}$)

Table 1: Experimental (E_{exp}) and calculated (E_{calc}) band centers of the lowest spin-vibronic states of the $\tilde{X}^+$ ^2E ground state of CH_3Cl^+. Γ_{ves} represents the spin-vibronic symmetry in the $C^2_{3v}(M)$ spin-double group.

	this work	Ref. [5]	Ref. [1]		Ref. [8] (TPES)
E_{I} / eV	11.28963(6)	11.290(5)	11.289(3)		11.296(15)
$a\zeta_{\mathrm{e}}d_{j=1/2,v=0}$ / cm^{-1}	-217.5(2.0)	-630(40)	-218(24)		-161(120)
			$^2E_{3/2}$	$^2E_{1/2}$	
ω_3 / cm^{-1}	647.5(5.0)	871(40)	637(24)	669(24)	613(120)
$a\zeta_{\mathrm{e}}d_{j=1/2,v_3=1}$ / cm^{-1}	-241.9(5.0)	-679(40)	-250(24)		-
ω_6 / cm^{-1}	1059.5(8.0)	-	887(24)	855(24)	839(120)
$a\zeta_{\mathrm{e}}d_{j=3/2,v=1}$ / cm^{-1}	-210.3(8.0)	-	-186(24)		-161(120)
$a\zeta_{\mathrm{e}}d_{j=1/2,v=1}$ / cm^{-1}	209.1(10.0)	-	186(24)		161(120)
ω_5 / cm^{-1}	(1484)$^{(a)}$	1550(40)	1557(24)	1532(24)	-
$a\zeta_{\mathrm{e}}d_{j,v_5=1}$ / cm^{-1}	-	-630(40)	-193(24)		-
ω_2 / cm^{-1}	1554.2(10.0)$^{(a)}$	1514(40)	1073(24)	-	-
$a\zeta_{\mathrm{e}}d_{j=1/2,v_2=1}$ / cm^{-1}	-217.5(10.0)$^{(b)}$	-	-		-

[a] Assignment tentative.

[b] Kept fixed at the value determined for the origin band.

Table 2: Adiabatic ionization energy E_{I}, spin-orbit splittings and harmonic frequencies of the vibrational modes of the $\tilde{X}^+$ $^2E \leftarrow \tilde{X}$ $^1A_1$ PFI-ZEKE photoelectron spectrum of CH_3Cl determined using values of $a = -645$ cm^{-1}, $\zeta_{\mathrm{e}} = 0.35$ and $D_6 = 0.009$, and comparison to results obtained in earlier works.

	$A^+\zeta_{ev}/cm^{-1}$	A^+/cm^{-1}	B^+/cm^{-1}	ζ_{ev}	ζ_e	$d_{j,v}$
$0_0^0\ j=1/2$	1.95(5)	5.79(+0.06;-0.15)	0.46(2)	0.346(10)	0.35(4)	0.963(20)
$6_0^1\ j=3/2$				0.53(21)	0.35(4)	0.931(20)
$6_0^1\ j=1/2$				-0.13(20)	0.35(4)	-0.926(20)

Table 3: Molecular parameters describing the E ⊗ e Jahn-Teller effect along the mode ν_6 in the $\tilde{X}^{+2}E$ ground state of CH_3Cl^+ derived from the rotational analysis of the photoelectron spectrum of the spin-orbit-split 0_0^0 and 6_0^1 bands, with $a = -645(5)$ cm^{-1}.